J Nanopart Res (2022) 24: 87
https://doi.org/10.1007/s11051-022-05462-y

RESEARCH PAPER

Assessment on thermal safety of aluminum hydroxide doping hydrophobic silica aerogels

Mengtian Sun · Zhi Li · Yan Zhang · Xiaoxu Wu · Long Shi · Qiong Liu · Ming Li

Received: 6 November 2021 / Accepted: 23 March 2022 / Published online: 15 April 2022

Abstract The thermal safety of hydrophobic silica aerogels (SA) attracts much concern in the field of heat insulation. It is urgent to develop SA composites with excellent thermal insulation properties to meet the current demands for efficient thermal insulation materials. In this work, alumina hydroxide (AH) doping SA (SA/AH) composites were prepared to enhance the thermal safety of hydrophobic SA. The microstructures and FTIR spectra of SA/AH indicate that it is the physical combination between SA and AH. The lower density of 0.11 g/cm^3 and the low thermal conductivity of 25.4 mW/(m·K) are still maintained despite of a slight increase with the AH content. The TG-DSC results demonstrate that the introduced AH improves the onset temperature of the thermal oxidation of Si-CH_3 groups by 55.2 °C. Furthermore, the oxidation kinetics verifies that the apparent activation energy of SA/AH4 (20% AH content) is much greater than that of the pure SA, indicating the thermal oxidation of Si-CH_3 groups in the SA/AH requires more energy to be triggered. The GCV of SA/AH4 is 8.44 MJ/kg, which is 29.6% lower than that of pure SA. The heat release rate (HRR), peak heat release rate (pHRR), and total heat release rate (THR) of SA/AH are significantly reduced. From the perspective of CO and CO_2 production during the combustion process, the smoke toxicity of SA/AH is significantly lower than that of the pure SA. Thus, this work concludes that doping AH is feasible and effective to improve the flame resistance of hydrophobic SA, which provides a technical basis for developing hydrophobic SA composites with enhanced thermal safety.

Keywords Hydrophobic silica aerogel · Aluminum hydroxide · Thermal stability · Flame resistance · Direct post-doping · Nanostructure · Insulation

M. Sun · Z. Li (✉) · Y. Zhang · Q. Liu (✉) · M. Li
School of Resources and Safety Engineering, Central South University, 410083 Changsha, People's Republic of China
e-mail: lizhi89@csu.edu.cn

Q. Liu
e-mail: liuqiong@csu.edu.cn

X. Wu
School of Economics and Management, Changsha University, 410003 Changsha, People's Republic of China

L. Shi
State Key Laboratory of Fire Science, University of Science and Technology of China, Hefei, Anhui 230027, People's Republic of China

Introduction

Hydrophobic silica aerogel (SA) is a nanoporous material, composed of mesopores (2–50 nm) and cross-linked SiO_2 nanoparticles (Zhao et al. 2020; Smith et al. 1998; Hsing and Schubert 1998). It shows a lot of applications in the thermal insulation field, such as building walls (Baetens et al. 2011;

Cuce et al. 2014), industrial pipelines (Villasmil et al. 2019), and spacecraft (Bheekhun et al. 2013; Randall et al. 2011). At present, hydrophobic SA has been considered one of the worldwide research hotspots regarding new efficient thermal insulation materials (Koebel et al. 2012).

Hydrophobic SA is formed by grafting organic groups onto silica skeletons through surface modification (Li et al. 2020), which effectively prevent water from invading the nanoporous network structure of SA. The hydrophobicity helps SA maintain an excellent thermal insulation performance for a long time. It is worthy to note that these organic groups not only endow SA with the hydrophobicity but also bring potential thermal hazards (Begag et al. 2008). But their flammability is usually ignored, especially under the continuously increasing thermal insulation applications. Nowadays, more and more attention has been attracted to this issue. For instance, Li et al. (2017) studied the flammability of the glass fiber membrane reinforced hydrophobic SA composites and found that the synthetic parameters had a significant impact on the fire risk of the SA compositions. Ghazi Wakili et al. (Ghazi Wakili and Remhof 2017) demonstrated that the exothermic reaction of the hydrophobic methyl groups was the main cause of the temperature rise of the ceramic fiber/aerogel composites. Further study indicates that the hydrophobic SA undergo the thermal decomposition (i.e., thermal oxidation) with releasing combustible gases, when suffering from a high temperature or heat flux (Li et al. 2016; Wu et al. 2020a). According to what mentioned above, the thermal safety of hydrophobic SA in their practical applications is seriously impaired due to the introduced organic hydrophobic groups. Hence, lowering the flammability or improving the flame retardancy is an urgent task for expanding the application fields and markets of hydrophobic SA.

He et al. (2019) analyzed the pyrolysis process of hydrophobic methyl group by TG-DSC, and the study showed that the thermal stability of SiO_2 aerogel can be improved by heat treatment at different temperatures. Some researchers enhance the thermal insulation properties and mechanical properties of aerogels by adding micro-sized mineral powders (such as carbon nanotubes (Patil et al. 2020; Adhikary et al. 2021a), SiC (Chen et al. 2020), etc.) and fibers with high extinction coefficient (Liu et al. 2020) (such as ceramic fibers (Tang et al. 2016), silicon fibers, etc.) in SiO_2 aerogel matrix (Adhikary et al. 2021b). At present, adding flame retardants is one of the common methods to improve the flame retardancy of materials. Hydroxides, e.g., $Al(OH)_3$ and $Mg(OH)_2$, are the common inorganic flame retardants. In this regard, Sánchez-Soto et al. (Wang et al. 2013) suggested that the heat released rate of poly(vinyl alcohol)/clay aerogel composites could be reduced by adding the aluminum hydroxide (AH) or ammonium polyphosphate (APP). Li et al. (2019) directly introduced aluminum hydroxide and magnesium hydroxide into the wet silica gels during the sol–gel stage and successfully decreased the flammability of the final hydrophobic SA.

In general, in view of the strict requirements in special fields such as pipeline insulation, developing hydrophobic silica aerogels with good thermal stability and flame retardancy is very urgent and still in great challenges. When introducing the additives into the native materials or reaction systems to achieve certain functions, a compatible, economical, and convenient method is always expected without changing the original preparation technology too much. This demand also occurs to the process of solving the flammability of hydrophobic SA. Therefore, it is urgent to find a method to improve the flame retardancy of SA without changing the existing preparation method of SA. The direct post-doping method is simple and effective, and provides a new idea for improving the thermal stability of hydrophobic SiO_2 aerogels.

In this study, we devote to investigating the feasibility of using aluminum hydroxide (AH) to enhance the flame retardancy of hydrophobic SA. Considering the compatibility with the existing preparation technology of SA, a direct post-doping is employed to modify the industrial-grade hydrophobic SA in this work. For this purpose, the microstructure, basic physicochemical properties, thermal and combustion properties, and oxidation kinetics of AH doped hydrophobic SA (SA/AH) are studied in detail. Furthermore, the effect of the AH doping content is also explored. At last, this work reveals the flame retardant mechanism of AH to decrease the flammability of hydrophobic SA and confirm the feasibility of using AH as the flame retardant by the direct post-doping.

Materials and methods

Preparation

In order to prevent SA and AH from being stratified due to the different density during mixing, we put some amount of SA and AH into a PE bag for preliminary mixing, and then the mixture was ground by a ball mill at 100 rpm for 1 h to generate the SA/AH composites. Pure SA was processed under the same conditions for comparison. The SA/AH composites with AH content of 5%, 10%, 15%, and 20% were named as SA/AH1, SA/AH2, SA/AH3, and SA/AH4-(Zhang et al. 2021). SA synthesized in the laboratory was used to study the gross calorific value and combustion behaviors of SA/AH composites. Commercial SA was used in other parts of the experiment of SA/AH composites.

Characterization methods

The tap density (ρ_t) of pure SA and SA/AH composites was measured by rotating the vibrating meter (ZS-202, Liaoning Instrument Research Institute, China) at 300 rpm for 10 min. The porosity of SA/AH composites was determined by Eq. (1):

$$Porosity = \left(1 - \frac{\rho_t}{(1-c)\rho_{sio_2} + c\rho_{AH}}\right) \times 100\% \quad (1)$$

where ρ_{sio_2} is the skeletal density of SA (generally 2.2 g/cm^3) and ρ_{AH} is the density of AH (about 2.4 g/cm^3), and c is the mass content of AH.

The micromorphology of the pure SA and SA/AH composites was characterized by field emission scanning electron microscopy (SEM, Zeiss Sigma 300). The N_2 sorption isotherms were measured using a Quadrasorb SI-3MP analyzer at 77 K. The pore size distribution (PSD), pore volume, and specific surface area were measured by automatic surface area and porosity analyzer (Quantachrome, AUTOSORB IQ) using the Barrett-Joyner-Halenda (BJH) (Li et al. 2019) and the Brunauer–Emmett–Teller (BET) method (Ozawa 1992). The particle size distribution of the samples was evaluated by the particle size analyzer (Malvern Mastersizer 3000, England). FT-IR spectrum (FTIR, Thermo Nicolet iS50) was recorded within 500–4000 cm^{-1} using KBr pellet pressing technique. The contact angles were obtained by dropping 5 ul water on the samples' surface using an automatic contact angle measuring instrument (Guangdong Aisry Instrument Technology Co., Ltd, ASR-705S). The obtained photographs were analyzed by the image analysis software, ImageJ (Schneider et al. 2012).

The thermal conductivities of the SA/AH composites were measured by transient hot-wire method using a thermal conductivity analyzer (Xiaxi, TC-3000E). The crystalline phase changes of pure SA and SA/AH4 before and after the pyrolysis were studied by X-ray Diffractometer (XRD, Bruker D8 advance) at a speed of 5°/min from 10 to 80°.

The thermal stability was investigated by Thermogravimetry and Differential Scanning Calorimeter (TG-DSC, SDT65, Waters) from room temperature to 1000 °C in air at a heating rate of 20 °C/min. The thermal kinetics of the pure SA and the SA/AH4 were analyzed based on the TG data at different heating rates of 10 °C/min, 20 °C/min, and 40 °C/min in the atmosphere of nitrogen. The apparent activation energies were calculated by the Kissinger–Akahira–Sunose (KAS) method (Ozawa 1992) and Flynn–Wall–Ozawa (FWO) method (Doyle 1962). The combustion behaviors of pure SA and SA/AH4 were tested with a cone calorimeter under a heat flux of 35 kW/m^2.

Results and discussion

Micromorphology

Figure 1 shows the microstructures of the pure SA, AH, and SA/AH4. In Fig. 1a, the pure SA has a typical porous network structure and the silica skeleton is composed of cross-linked silica nanoparticles. In Fig. 1b, the AH is made up of cumulated micron-sized particles. Figure 1c shows the morphology of the SA/AH4, in which the brighter particles (AH) disperse around the lumps (SA). From the composition structure, it is considered that there is no chemical reaction between the pure SA and AH particles and it is actually a simple physical dispersion between them.

Figure 2a exhibits the N_2 sorption isotherms of the SA/AH composites with different AH contents. In Fig. 2a, the adsorption capacity of SA/AH composites are larger than that of pure SA, which may be caused by the collapse of some pores in SA/AH. From the

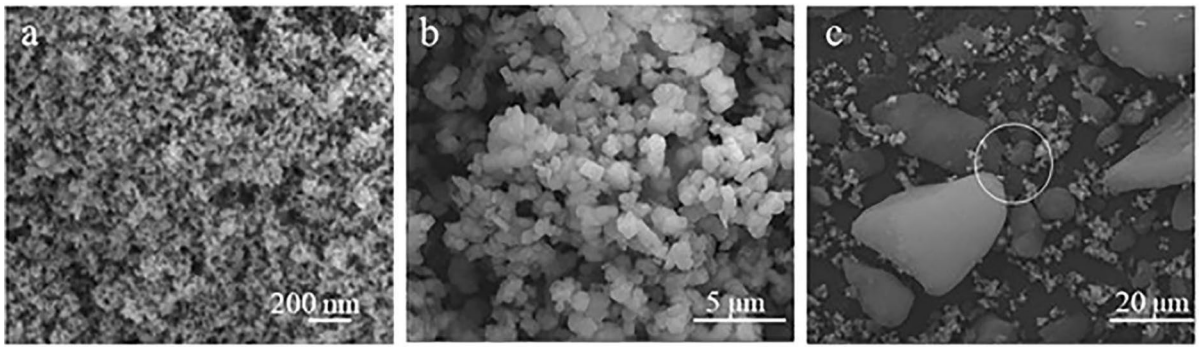

Fig. 1 SEM images of **a** pure SA, **b** AH, and **c** SA/AH4

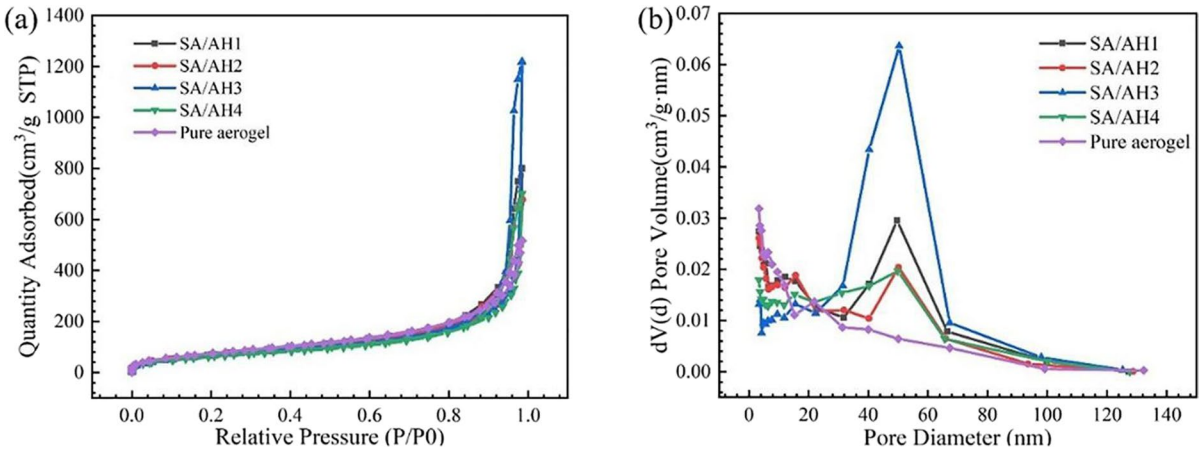

Fig. 2 **a** N_2 sorption isotherms and **b** pore size distribution of pure SA and SA/AH1-4

hysteresis loop in Fig. 2a, we can speculate that it is because the micropores in the SA/AH composites are collapsed into mesopores (Lei et al. 2017), resulting in an increase in pore size and a decrease in the specific surface area of SA/AH. According to the IUPAC classification (Rojas et al. 2002), all the samples display the IV-type sorption isotherms with the H3-type hysteretic loop. These results indicate that these samples are still materials with mesoporous structure and have the slit-shaped pores (He et al. 2021).

Figure 2b shows the pore size distribution of pure SA and SA/AH composites, in which the pore sizes of the SA/AH1-4 mainly range within 20–70 nm. Compared to the pure SA, the most probable pore sizes of the SA/AH shift to the larger pore size (about 50 nm). The detailed pore parameters of these samples are listed in Table 1. It finds that the average pore size of SA/AH composites extends and the specific surface area decreases with the AH content increasing. It further speculates that the AH not only acts as a dopant but also plays a role of abradant. During the grinding process, the collisions between the AH and SA render the collapse of the porous network of SA, which

Table 1 Textural properties of pure SA, $Al(OH)_3$ and SA/AH dopped by different AH contents

Samples	Specific surface area (m^2/g)	Pore volume (cm^3/g)	Average pore size (nm)
Pure SA	298	0.801	10.9
SA/AH1	275	1.206	18.0
SA/AH2	270	0.991	15.5
SA/AH3	249	0.690	11.5
SA/AH4	241	1.046	18.0
$Al(OH)_3$	2.74	0.008	12.0

further leads to the decreasing of the specific surface area.

Porosity, density, thermal conductivity, and hydrophobicity

Figure 3 presents the porosity, density, and thermal conductivity of the SA/AH composites with various AH contents between 5 and 20%. In Fig. 3a, at 5% AH doping content, the density of the SA/AH maintains almost unchanged, and then increases dramatically as the doping content grows. As it is reported that the electrostatic repulsion extends the particle intervals among the AH and SA particles and SA/AH composite particles (Li et al. 2019), this effect leads to the decrease of the density of the SA/AH to some extent. Consequently, the density of the SA/AH with 5% AH keeps almost unchanged. With the AH content increasing, the large density of the AH (about 2.4 g/cm^3) is hard to be counteracted by the mentioned effect of electrostatic repulsion. As a result, the dramatic rise occurs on the density of the SA/AH. In spite of the increasing density, all the SA/AH composites' porosities are greater than 95% within a doping amount of 5–20% and present an opposite trend of the density.

As shown in Fig. 3b, pure SA's thermal conductivity is 24.8 mW/(m·K), while the thermal conductivity of the SA/AH grows slowly from 24.9 to 25.4 mW/(m·K) along with the AH content within 5–20%. As the AH doping content increases, more heat transfer passages are provided, causing a rise in thermal conductivity of the SA/AH composites. Nonetheless, the thermal conductivity of the SA/AH composites with the AH content ranging at 0–20% is still lower than that of the still air at room temperature, about 26 mW/(m·K). This result indisputably indicates that the obtained SA/AH composites still own excellent thermal insulation performance.

Figure 4 is the contact angles of the SA/AH composites with AH contents ranging from 5 to 20%. Compared to the contact angle of the pure SA (145°), the contact angles of the SA/AH are obviously smaller (131–135°). This diminution of the contact angle is deemed to be related to the hydrophilia of AH. Even so, the contact angles of all samples are greater than 130°, and they all present a good hydrophobicity. That is to say, the introduction of AH does not impair the hydrophobicity of SA/AH too much. And it also suggests that the SA/AH can still meet the requirement of moisture resistance.

Figure 5 presents the infrared spectrometry of the pure SA and the SA/AH4. The peaks around 1650 cm^{-1} and the broad absorption peak around 3440 cm^{-1} are ascribed to the asymmetric stretching and bending vibration of -OH groups, respectively (Al-Oweini and El-Rassy 2009; Shi et al. 2022). The symmetric and asymmetric stretching vibrations and the shear bending vibration of the C-H bonds in -CH_3 groups are observed around 2980–2880 cm^{-1} and 1409 cm^{-1} (Parvathy Rao et al. 2007), separately. The peaks at 845 and 758 cm^{-1} belong to the Si–C

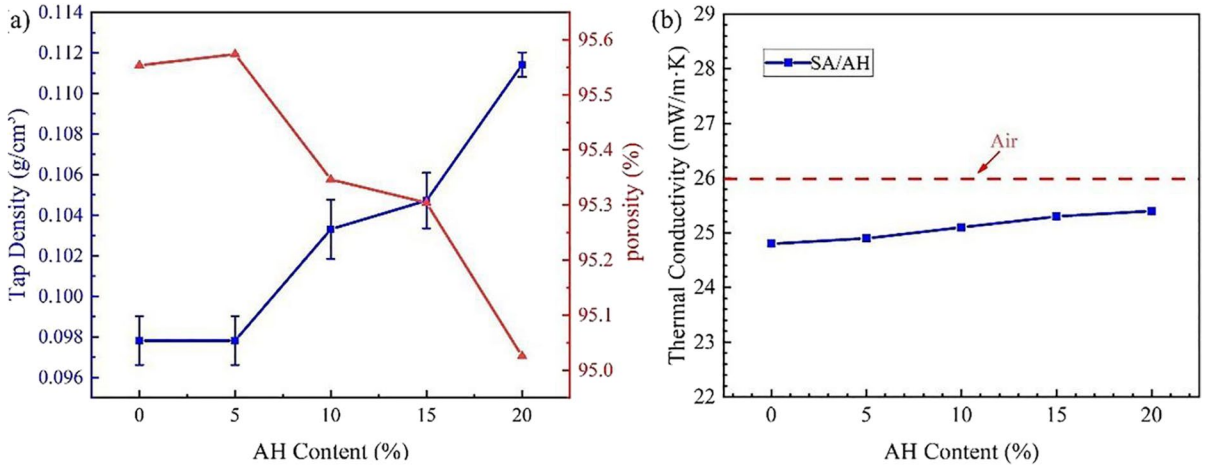

Fig. 3 SA/AH composites' **a** porosity and density, and **b** thermal conductivity

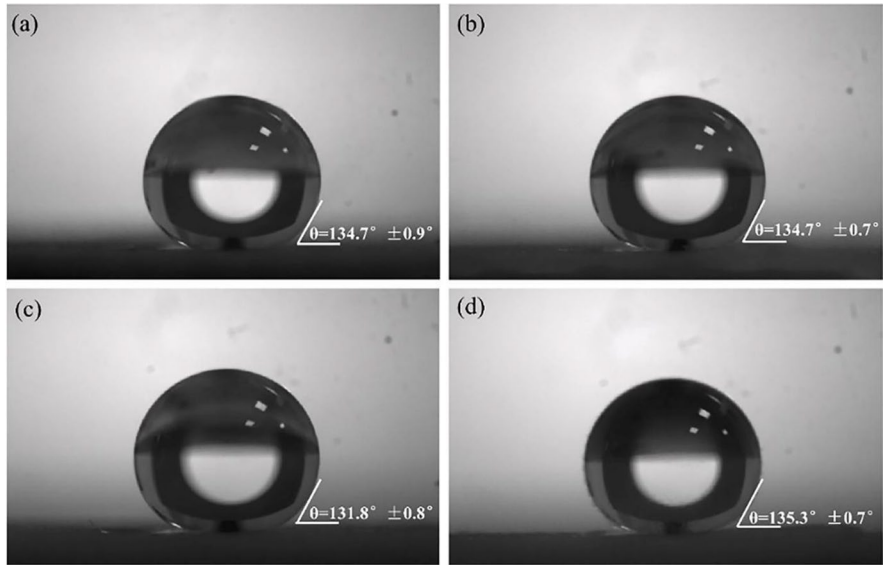

Fig. 4 Contact angles of **a** SA/AH1, **b** SA/AH2, **c** SA/AH3, and **d** SA/AH4

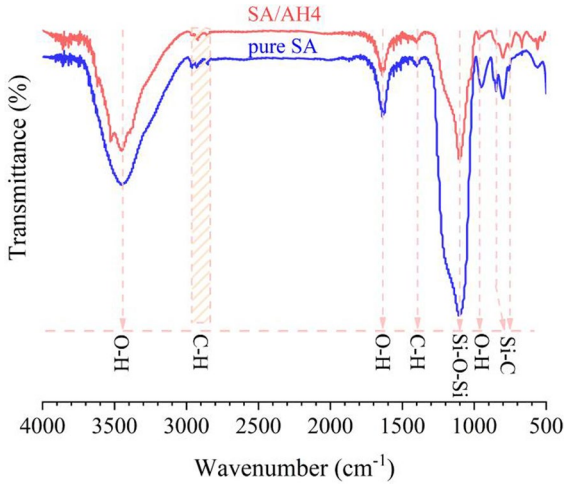

Fig. 5 The infrared spectrometry of the pure SA and SA/AH4

bonds (Bhagat and Rao 2006), indicating the presence of Si-$(CH_3)_3$ groups introduced by surface modification. These remained Si-$(CH_3)_3$ groups on the silicon skeletons become the chemical foundation of the hydrophobicity (Wu et al. 2020b), which makes SA resist water and moisture. The prominent peaks at 1085 cm^{-1} and 790 cm^{-1} correspond to the antisymmetric stretching vibration and symmetric stretching vibration modes of Si–O-Si bonds (Li et al. 2015). Comparing the IR spectra of the two, it finds that the SA and SA/AH4 display similar spectra without any new chemical bonds. It further indicates that the formation of the SA/AH is the physical combination between SA and AH (Zhang et al. 2021).

Thermostability analysis

The thermogravimetric and differential scanning calorimetric analysis (TG-DSC) curves of the pure SA and SA/AH4 are presented in Fig. 6. The TG curves of the pure SA (Fig. 6a) and SA/AH4 (Fig. 6b) have a small weight loss at around 100–150 °C which is due to the removal of moisture and residual organic solvent from the system (He et al. 2019). In Fig. 6a, the pure SA shows a distinct weight loss (stage II) when the temperature goes above 360 °C. This weight loss is usually regarded as the thermal decomposition of the Si-CH_3 groups introduced by surface modification (Li et al. 2018). In Fig. 6b, the SA/AH4 appears two considerable main transitions. The first weight loss occurs at the temperature of around 245 °C (stage I), during which AH undergoes thermal decomposition reaction. The thermal decomposition reaction of AH is an endothermic reaction, which results in insufficient heat during the reaction process. When the temperature is up to about 420 °C, the oxidative decomposition of the Si-CH_3 groups begins, which leads to the second weight loss (stage II).

It was observed from the DSC curves that the pure SA shows one exothermic peak, while the SA/AH4 shows an endothermic peak and an exothermic peak, separately. As mentioned above, the exothermic peak

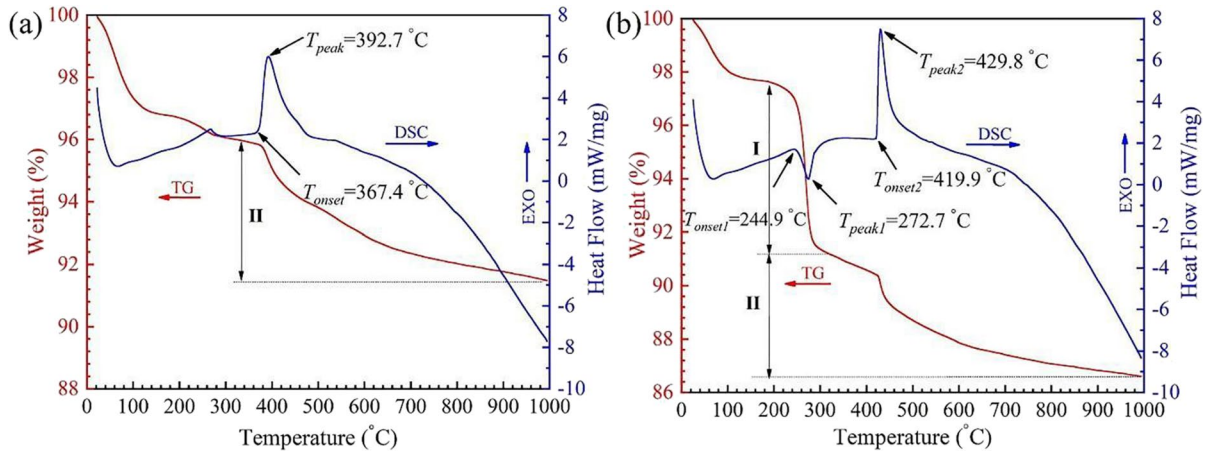

Fig. 6 Thermogravimetric and differential scanning calorimetric analysis for **a** pure SA and **b** SA/AH4

Table 2 The detailed DSC parameters of the pure SA and SA/AH4

Sample	Stage I		Stage II	
	T_{onset} (°C)	T_{peak} (°C)	T_{onset} (°C)	T_{peak} (°C)
SA	\	\	364.7	392.7
SA/AH4	244.9	272.7	419.9	429.8

is attributed to the oxidative decomposition of methyl groups on the skeletons. Correspondingly, the endothermic peak belongs to the dehydration reaction of the AH (Bangi et al. 2012).

The thermal stability is commonly indicated by the onset temperature (T_{onset}) and the peak temperature (T_{peak}) of the exothermic reaction. Now, these parameters have been listed in Table 2. At the stage I of the SA/AH4, the T_{onset} for the dehydration reaction of the AH is 244.9 °C and the T_{peak} is 272.7 °C. This process needs to absorb energy to trigger the dehydration reaction, just corresponding to the endothermic peak. More differences are observed at the stage II of the SA and SA/AH4. For the pure SA, the T_{onset} for the thermal oxidation of Si-CH_3 is 367.4 °C, while that for the SA/AH reaches as high as 419.9 °C. Namely, the introduction of 20% AH improves the T_{onset} by 52.5 °C. From the view of the T_{peak}, it is enhanced by 37.1 °C.

Compared with the pure SA, the SA/AH4 postpones the thermal oxidation of the Si-CH_3 groups with the improved T_{onset} and T_{peak}. Therefore, it confirms that the introduction of AH can efficiently hinder the thermal oxidation decomposition of Si-CH_3 groups, indicating that compared with the pure SA, the SA/AH composites show a relatively lower thermal hazard potential and the thermal stability of them is improved.

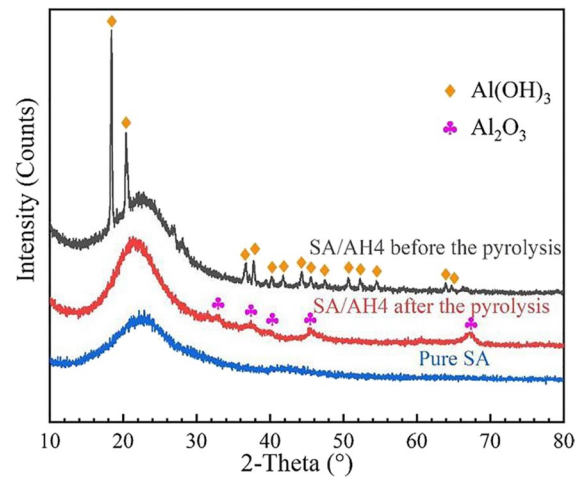

Fig. 7 XRD patterns of pure SA and SA/AH4 before and after the pyrolysis

Composition before and after the pyrolysis

Figure 7 shows the XRD patterns of the pure SA and SA/AH4 before and after the pyrolysis. All the three samples show a broad peak at the low diffraction angle of 20–25° that is the amorphous diffraction peak, indicating the pure SA and SA/AH4

before and after the pyrolysis are all amorphous structures (Huang et al. 2017). After the pure SA being doped with AH, the characteristic peaks of AH can be observed and the characteristic peaks of Al_2O_3 appear after the pyrolysis of the SA/AH. It indicates that the main pyrolysis product is Al_2O_3 and the produced Al_2O_3 and SiO_2 do not react with each other even under a high temperature of 1000 °C. It is worthy to point out that Al_2O_3 is a high-temperature material, which can hinder the heat or fire transfer to some extent. From this view, the generated Al_2O_3 is effective in inhibiting the pyrolysis of SA.

Oxidation kinetics analysis

In Fig. 8, the optimum fitting lines are determined by the least square method and most of the fitting lines exhibit good linearity. The apparent activation energies (E_α) are calculated based on the slopes of the corresponding fitted lines.

In Fig. 9a, the pyrolysis process of the pure SA in accordance with E_α can be roughly divided into two stages. At stage I ($\alpha < 0.4$), E_α increases significantly. As discussed above, this stage is mainly due to the vaporization of residual organic solvents and water in the SA. For the liquid on the surface of silica skeletons and in the open pores, they are easy to be evaporated. However, it is not easy for the evaporation of

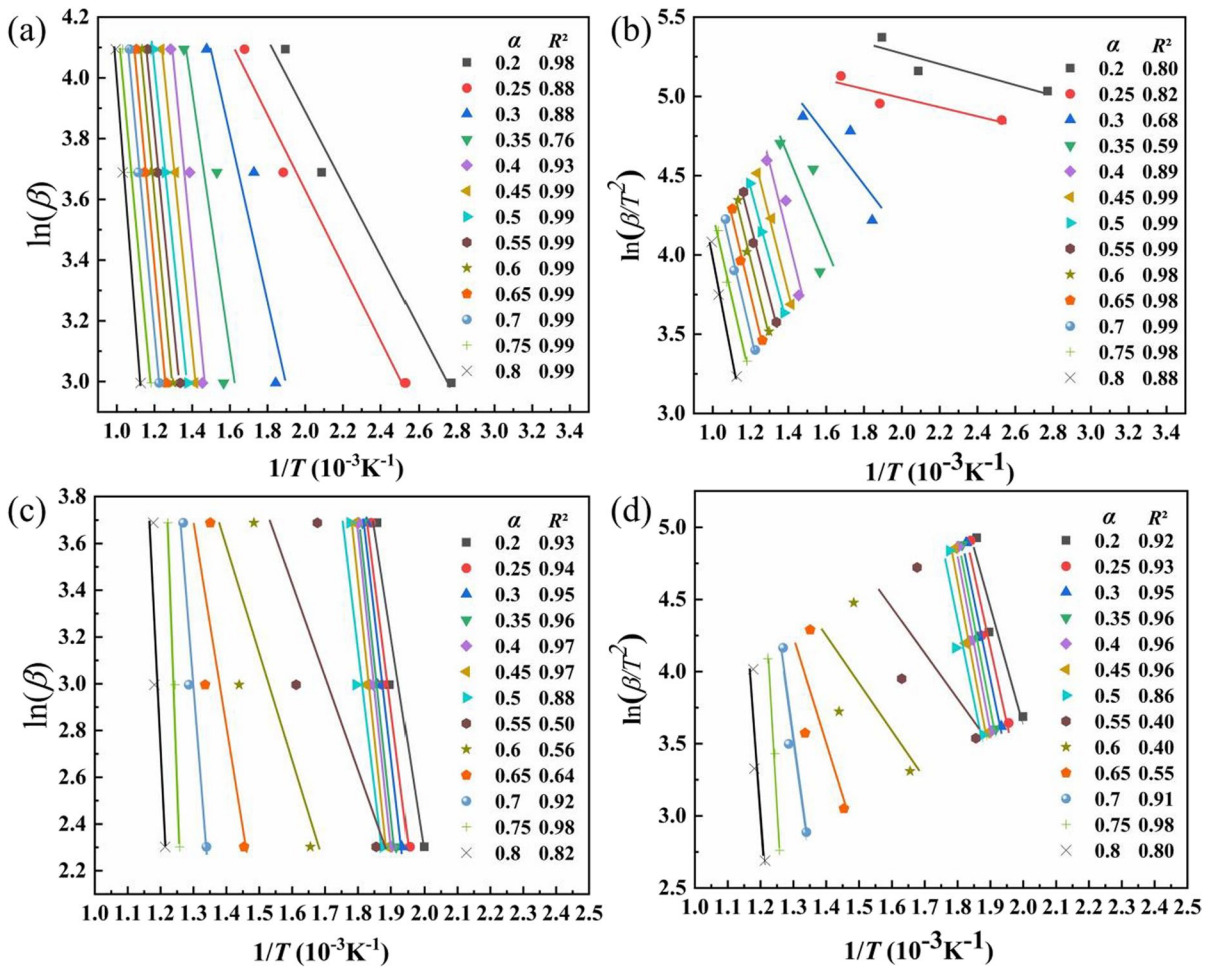

Fig. 8 Fitting lines based on the FWO method (**a** and **c**) and the KAS method (**b** and **d**), thereinto, **a** and **b** is the pure SA and **c** and **d** is the SA/AH4, respectively

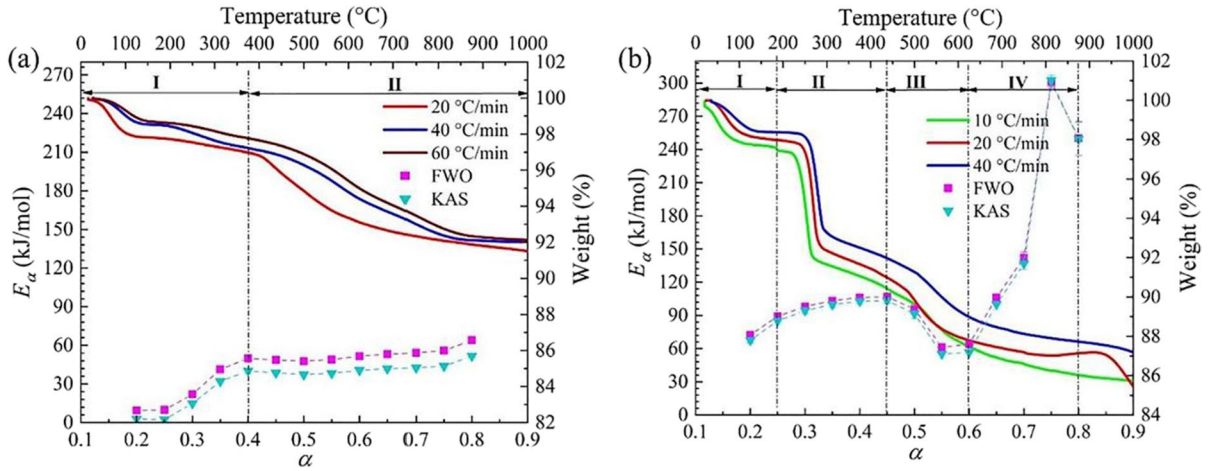

Fig. 9 E_α versus α for **a** the pure SA and **b** SA/AH4

the liquid inside the silica skeletons themselves and in some closed structures. As a result, more energy is needed to drive those liquid to evaporate.

At stage II ($\alpha \geq 0.4$), E_α remains nearly constant at first and then slightly grows up to 62 kJ/mol. The oxidative decomposition of the methyl groups as well as the polycondensation of the silanol groups mainly occur at this stage. At the stage of $\alpha \in$ (0.7, 0.8), a majority of the Si-CH_3 groups have been oxidated and the remained and newly formed Si–OH groups keep conducting the condensation reaction under a higher temperature (He et al. 2019). Hence, E_α rises a little bit.

The pyrolysis process of the SA/AH4 can be split into four stages in Fig. 9b, which is more complicated than that of the pure SA. Now the detailed pyrolysis process of the SA/AH is discussed as follow.

At stage I ($\alpha < 0.25$), E_α increases slightly, which is the same with that of the stage I of the pure SA, corresponding to the vaporization of the remained liquid.

At stage II ($0.25 < \alpha < 0.45$), E_α also goes up slightly. This stage just corresponds to the dehydration of AH and the reaction equation is listed in Eq. (2). Note that the dehydration of AH is an endothermic reaction. With this reaction going on, it takes more energy to maintain the dehydration reaction. As a consequence, the apparent activation energy rises up.

$$Al(OH)_3(s) === Al_2O_3(s) + H_2O(g) \quad (2)$$

At stage III ($0.45 < \alpha < 0.6$), the thermal oxidative decomposition of Si-CH_3 groups and the polycondensation of Si–OH groups occur simultaneously on the silica skeletons. At this stage, E_α obviously decreases to the minimum of 63.9 kJ/mol, indicating that the oxidation of the methyl groups tends to be easier to occur with the reaction proceeding. In spite of that, the minimum apparent activation energy of the SA/AH4 is still higher than that of the pure SA.

At stage IV ($0.6 < \alpha < 0.8$), a small number of the remained Si–OH groups keep condensation, while other reactions, such as the reaction between SiO_2 and Al_2O_3, are hard to occur. This is consistent with the literature that Al_2O_3 has excellent high-temperature properties and can maintain its initial structure at a high temperature above 1300 °C (Wagle and Yoo 2020). Correspondingly, the apparent activation energy rises dramatically from 63.9 to 300 kJ/mol and then decreases to 250.1 kJ/mol, which means the tough reaction at this stage requires more energy to be triggered. Therein, the decrease of E_α is related to the phase change of produced SiO_2.

As a whole, E_α of the pure SA (Fig. 9b) is significantly lower than that of the SA/AH composites (Fig. 9a) at the same conversion rate (α), which suggests that the thermal decomposition reaction of the SA/AH4 is relatively difficult to occur. To be specific, the dehydration of the AH generates Al_2O_3 and H_2O. This dehydration itself and the evaporation of the produced water absorb energy form the reaction system, which leads to the cooling effect. Besides, the formed water vapor dilutes the oxygen, reducing the oxygen concentration around the silica skeletons. Both the

cooling effect and dilution effect benefit to inhibiting the oxidation of the methyl groups on the silica skeletons. Furthermore, the generated Al_2O_3 is a high temperature material, which can block the heat or fire transfer in the reaction system. As a consequence, the onset decomposition temperature of the Si-CH_3 groups in the SA/AH composites is significantly improved and E_α at stage III is also enhanced accordingly. Thereby, it can conclude that the introduction of AH can efficiently reduce the thermal hazards of hydrophobic SA.

Gross calorific value

Gross calorific value (GCV) reflects the total heat released of a material after complete combustion (Rhen 2004; Llorente and Garcia 2008). As shown in Fig. 10, the GCV of pure SA was 12.0 MJ/kg, while that of SA/AH4 decreased by 29.6%, reaching to 8.44 MJ/kg. It is clearly known based on the experimental data that the GCV of SA is reduced with doping the non-combustible AH, that is, the heat released by SA/AH after complete combustion is reduced. Thence, the SA/AH has lower potential thermal hazard than that of the pure SA.

Combustion behaviors

To further study the impact of AH on the flame retardant performance of SA, trimethylchlorosilane (TMCS) modified SiO_2 aerogels prepared in our laboratory are employed in this study through the cone calorimetry experiments. Cone calorimetry is based on the principle of oxygen consumption. It can provide heat release rate (HRR), total heat release (THR), and other parameters close to the real combustion process, which is an effective method to study the combustion behavior of materials.

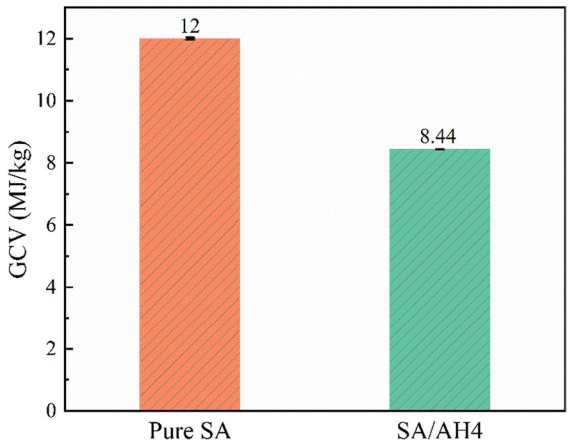

Fig. 10 GCV of pure SA and SA/AH4

Fire hazard analysis

The HRR and THR of pure SA and SA/AH4 are displayed in Fig. 11. After the SA and SA/AH4 are ignited, both their HRR increase sharply with reaching the peak heat release rate (pHRR), and then gradually decay until the final extinction. As it is known to us, the pHRR is one of the most important fire characteristic parameters of a material. It finds that the pHRR of SA decreases from 63.71 to 55.85 kW/m^2 with adding 20% AH. Correspondingly, both of the THR during the combustion process gradually ascend to the maximum and then keep almost unchanged. In the meantime, the THR of pure SA is 10.65 MJ/m^2, while that of SA/AH4 is only 7.0 MJ/m^2. From the above data, it finds that the HRR and THR of pure SA are always higher than those of SA/AH4 during the whole combustion process. That is to say, the addition of AH has a significant inhibitory effect on the combustion process of SA, which can greatly lower the fire hazard of SA.

Smoke toxicity analysis

Figure 12 reflects the CO production (COP) and CO_2 production (CO_2P) of pure SA and AH/SA4 during the whole combustion process. After the SA and SA/AH4 are ignited, both the COP and CO_2P move upward rapidly with reaching their peaks, and then decay until the fire is extinguished. These variations of the COP and CO_2P are similar with the HRR and the difference between the two is the time to the peaks. After ignition, it needs about 40 s to reach the pHRR, 60 s to reach the peak of CO_2P and 170 s to reach peak of COP. Because the CO_2 is mainly produced during the violent burning stage in spite of the 20 s delay, while the CO is primarily produced during the burning down stage.

Comparing the COP and CO_2P between the pure SA and SA/AH4, it finds that with doping 20% AH, the COP peak of SA decreases from 5.0×10^{-3} to 3.9×10^{-3} g/s, and the CO_2P peak of SA drops from

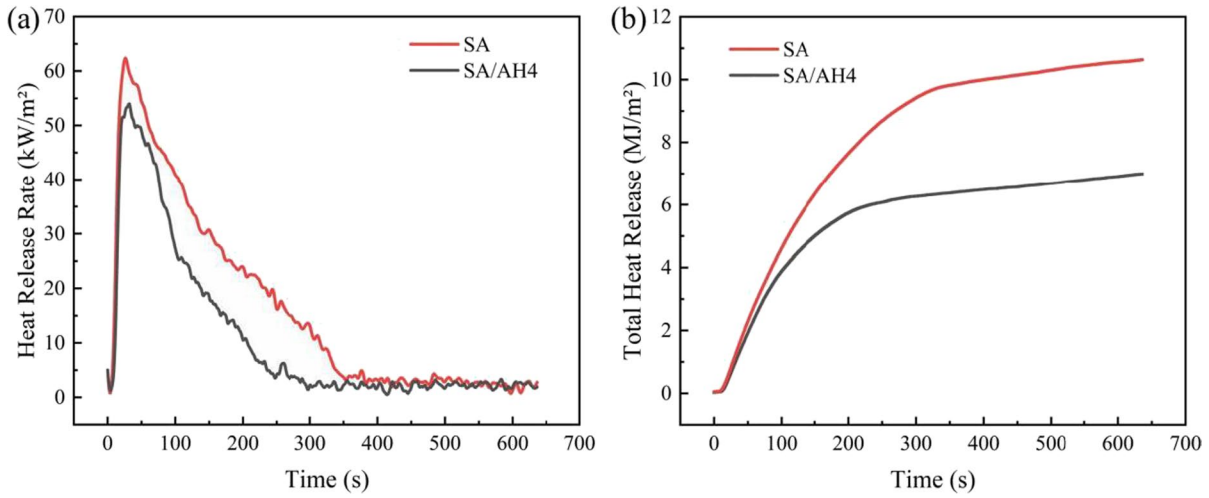

Fig. 11 HRR and THR of **a** the pure SA and **b** SA/AH4

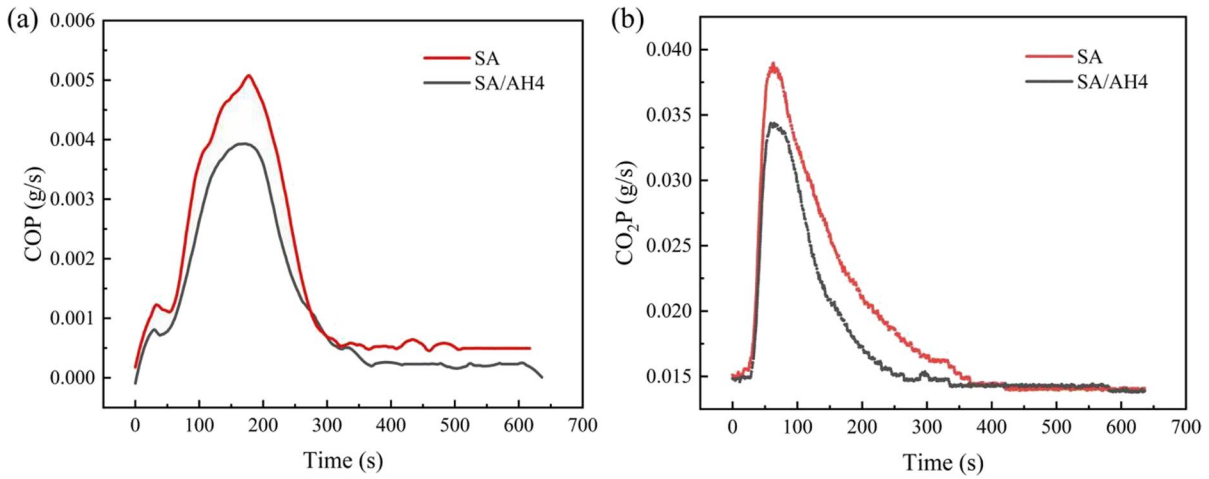

Fig. 12 Production of CO and CO_2 for **a** the pure SA and **b** SA/AH4

3.89×10^{-2} to 3.43×10^{-2} g/s. From the view of smoke suppression, it indicates that the introduction of AH can effectively reduce the production of CO and CO_2 during the combustion process.

Conclusions

Aiming to enhance the flame retardancy, we prepare the SA/AH composites by adding aluminum hydroxide (AH) to hydrophobic silica aerogels (SA). The microstructure and surface chemistry indicate that the SA/AH is formed by the physical combination of the SA and AH. The lower density and lower thermal conductivity are still maintained despite of the slight growth caused by the increasing AH content. The thermal analysis reveals the pyrolysis process of the SA/AH composites and finds that the onset temperature of the thermal decomposition of the methyl groups in SA/AH composites is improved. The oxidation kinetics point out that the apparent activation energy of the SA/AH4 composites is significantly higher than that of the pure SA. The GCV of SA/AH4 is 30% lower than that of pure SA. These three points

demonstrate that the introduction of AH can effectively reduce the thermal hazards of the hydrophobic SA. The heat release rate (HRR), peak heat release rate (pHRR), and total heat release (THR) of SA/AH decreased significantly compared to those of pure SA. The smoke toxicity of SA/AH was evidently less than that of the pure SA, evidenced by the decreased CO and CO_2 production rate during the combustion process. From the perspective of the microstructures, thermal properties, oxidation kinetics, and combustion behaviors, we conclude that the AH can effectively enhance flame retardant performance of hydrophobic SA without impairing the physicochemical properties too much.

Acknowledgements This work was supported by the National Natural Science Foundation of China (no. 51904336), the Natural Science Foundation of Hunan Province (no. 2020JJ4714), the Open Sharing Fund for the Large-scale Instruments and Equipments of Central South University (CSUZC202135), and the Fundamental Research Funds for the Central Universities (no. 202501003 and 202045001).

Declarations

Conflict of interest The authors declare that they have no conflict of interest.

References

Adhikary SK, Rudžionis Ž, Tučkutė S, Ashish DK (2021a) Effects of carbon nanotubes on expanded glass and silica aerogel based lightweight concrete. Sci Rep 11:2104. https://doi.org/10.1038/s41598-021-81665-y

Adhikary SK, Ashish DK, Rudžionis Ž (2021b) Aerogel based thermal insulating cementitious composites: a review. Energy Build 245:111058. https://doi.org/10.1016/j.enbuild.2021.111058

Al-Oweini R, El-Rassy H (2009) Synthesis and characterization by FTIR spectroscopy of silica aerogels prepared using several Si(OR)4 and R″Si(OR′)3 precursors. J Mol Struct 919:140–145. https://doi.org/10.1016/j.molstruc.2008.08.025

Baetens R, Jelle BP, Gustavsen A (2011) Aerogel insulation for building applications: a state-of-the-art review. Energy Build 43:761–769. https://doi.org/10.1016/j.enbuild.2010.12.012

Bangi UKH, Park C-S, Baek S, Park H-H (2012) Improvement in optical and physical properties of TEOS based aerogels using acetonitrile via ambient pressure drying. Ceram Int 38:6883–6888. https://doi.org/10.1016/j.ceramint.2012.07.051

Begag R, Fesmire JE, Sonn JH (2008) Nonflammable, hydrophobic aerogel composites for cryogenic applications, in: Koenig JR, Ban H (Eds.), Thermal Conductivity 29: Thermal Expansion 17, pp. 323-+.

Bhagat SD, Rao AV (2006) Surface chemical modification of TEOS based silica aerogels synthesized by two step (acid–base) sol–gel process. Appl Surf Sci 252:4289–4297. https://doi.org/10.1016/j.apsusc.2005.07.006

Bheekhun N, Abu Talib AR, Hassan MR (2013) Aerogels in aerospace: an overview. Adv Mater Sci Eng 2013:1–18. https://doi.org/10.1155/2013/406065

Chen Y, Li D, Xie X-Q, Gao Y, He Y-L (2020) Theoretical modeling and experimental validation for the effective thermal conductivity of moist silica aerogel. Int J Heat Mass Transf 147:118842. https://doi.org/10.1016/j.ijheatmasstransfer.2019.118842

Cuce E, Cuce PM, Wood CJ, Riffat SB (2014) Toward aerogel based thermal superinsulation in buildings: a comprehensive review. Renew Sustain Energy Rev 34:273–299. https://doi.org/10.1016/j.rser.2014.03.017

Doyle CD (1962) Estimating isothermal life from thermogravimetric data. J Appl Polym Sci 6:639–642. https://doi.org/10.1002/app.1962.070062406

Ghazi Wakili K, Remhof A (2017) Reaction of aerogel containing ceramic fibre insulation to fire exposure: reaction of aerogel containing insulation to fire. Fire Mater 41:29–39. https://doi.org/10.1002/fam.2367

He S, Huang Y, Chen G, Feng M, Dai H, Yuan B, Chen X (2019) Effect of heat treatment on hydrophobic silica aerogel. J Hazard Mater 362:294–302. https://doi.org/10.1016/j.jhazmat.2018.08.087

He S, Chen G, Xiao H, Shi G, Ruan C, Ma Y, Dai H, Yuan B, Chen X, Yang X (2021) Facile preparation of N-doped activated carbon produced from rice husk for CO2 capture. J Colloid Interface Sci 582:90–101. https://doi.org/10.1016/j.jcis.2020.08.021

Hsing N, Schubert U (1998) Aerogels-Airy Materials: Chemistry, Structure, and Properties. Angew Chem Int Ed 24. https://doi.org/10.1002/(SICI)1521-3773(19980202)37:1/2<22::AID-ANIE22>3.0.CO;2-I

Huang D, Guo C, Zhang M, Shi L (2017) Characteristics of nanoporous silica aerogel under high temperature from 950 °C to 1200 °C. Mater Des 129:82–90. https://doi.org/10.1016/j.matdes.2017.05.024

Koebel M, Rigacci A, Achard P (2012) Aerogel-based thermal superinsulation: an overview. J Sol-Gel Sci Technol 63:315–339. https://doi.org/10.1007/s10971-012-2792-9

Lei Y, Chen X, Song H, Hu Z, Cao B (2017) The influence of thermal treatment on the microstructure and thermal insulation performance of silica aerogels. J Non-Cryst Solids 470:178–183. https://doi.org/10.1016/j.jnoncrysol.2017.05.020

Li Z, Cheng X, He S, Shi X, Yang H (2015) Characteristics of ambient-pressure-dried aerogels synthesized via different surface modification methods. J Sol-Gel Sci Technol 76:138–149. https://doi.org/10.1007/s10971-015-3760-y

Li Z, Cheng X, Shi L, He S, Gong L, Li C, Zhang H (2016) Flammability and oxidation kinetics of hydrophobic silica aerogels. J Hazard Mater 320:350–358. https://doi.org/10.1016/j.jhazmat.2016.07.054

Li C, Cheng X, Li Z, Pan Y, Huang Y, Gong L (2017) Mechanical, thermal and flammability properties of glass fiber film/silica aerogel composites. J Non-Cryst Solids

457:52–59. https://doi.org/10.1016/j.jnoncrysol.2016.11.017

Li Z, Cheng X, Gong L, Liu Q, Li S (2018) Enhanced flame retardancy of hydrophobic silica aerogels by using sodium silicate as precursor and phosphoric acid as catalyst. J Non-Cryst Solids 481:267–275. https://doi.org/10.1016/j.jnoncrysol.2017.10.053

Li Z, Huang S, Shi L, Li Z, Liu Q, Li M (2019) Reducing the flammability of hydrophobic silica aerogels by doping with hydroxides. J Hazard Mater 373:536–546. https://doi.org/10.1016/j.jhazmat.2019.03.112

Li Z, Zhao S, Koebel MM, Malfait WJ (2020) Silica aerogels with tailored chemical functionality. Mater Des 193:108833. https://doi.org/10.1016/j.matdes.2020.108833

Liu H, Hu M, Jiao J, Li Z (2020) Geometric optimization of aerogel composites for high temperature thermal insulation applications. J Non-Cryst Solids 547:120306. https://doi.org/10.1016/j.jnoncrysol.2020.120306

Llorente MJF, Garcia JEC (2008) Suitability of thermo-chemical corrections for determining gross calorific value in biomass. Thermochim Acta 468:101–107. https://doi.org/10.1016/j.tca.2007.12.003

Ozawa T (1992) Estimation of activation energy by isoconversion methods. Thermochim Acta 203:159–165. https://doi.org/10.1016/0040-6031(92)85192-X

Parvathy Rao A, Rao AV, Pajonk GM (2007) Hydrophobic and physical properties of the ambient pressure dried silica aerogels with sodium silicate precursor using various surface modification agents. Appl Surf Sci 253:6032–6040. https://doi.org/10.1016/j.apsusc.2006.12.117

Patil SP, Shendye P, Markert B (2020) Molecular dynamics simulations of silica aerogel nanocomposites reinforced by glass fibers, graphene sheets and carbon nanotubes: a comparison study on mechanical properties. Compos B-Eng 190:107884. https://doi.org/10.1016/j.compositesb.2020.107884

Randall JP, Meador MAB, Jana SC (2011) Tailoring mechanical properties of aerogels for aerospace applications. ACS Appl Mater Interfaces 3:613–626. https://doi.org/10.1021/am200007n

Rhen C (2004) Chemical composition and gross calorific value of the above-ground biomass components of young Picea abies. Scand J Forest Res 19:72–81. https://doi.org/10.1080/02827580310019185

Rojas F, Kornhauser I, Felipe C, Esparza JM, Cordero S, Domínguez A, Riccardo JL (2002) Capillary condensation in heterogeneous mesoporous networks consisting of variable connectivity and pore-size correlation. Phys Chem Chem Phys 4:2346–2355. https://doi.org/10.1039/b108785a

Schneider CA, Rasband WS, Eliceiri KW (2012) NIH image to ImageJ: 25 years of image analysis. Nat Methods 9:671–675. https://doi.org/10.1038/nmeth.2089

Shi G, He S, Chen G, Ruan C, Ma Y, Chen Q, Jin X, Liu X, He C, Du C, Dai H, Yang X (2022) Crayfish shell-based micro-mesoporous activated carbon: Insight into preparation and gaseous benzene adsorption mechanism. Chem Eng J 428:131148. https://doi.org/10.1016/j.cej.2021.131148

Smith DM, Maskara A, Boes U (1998) Aerogel-based thermal insulation. J Non-Cryst Solids 225:254–259. https://doi.org/10.1016/S0022-3093(98)00125-2

Tang GH, Zhao Y, Guo JF (2016) Multi-layer graded doping in silica aerogel insulation with temperature gradient. Int J Heat Mass Transf 99:192–200. https://doi.org/10.1016/j.ijheatmasstransfer.2016.03.093

Villasmil W, Fischer LJ, Worlitschek J (2019) A review and evaluation of thermal insulation materials and methods for thermal energy storage systems. Renew Sust Energ Rev 103:71–84. https://doi.org/10.1016/j.rser.2018.12.040

Wagle R, Yoo JK (2020) Preparation of highly porous Al_2O_3 aerogel by one-step solvent-exchange and ambient-pressure drying. Int J Appl Ceram Technol 17:1201–1212. https://doi.org/10.1111/ijac.13455

Wang L, Sánchez-Soto M, Maspoch ML (2013) Polymer/clay aerogel composites with flame retardant agents: mechanical, thermal and fire behavior. Mater Des 52:609–614. https://doi.org/10.1016/j.matdes.2013.05.096

Wu X, Li Z, Joao G, Zhang Y, Huang S, Liu Q (2020a) Reducing the flammability of hydrophobic silica aerogels by tailored heat treatment. J Nanopart Res 22:83. https://doi.org/10.1007/s11051-020-04822-w

Wu X, Huang S, Zhang Y, Shi L, Luo Y, Deng X, Liu Q, Li Z (2020b) Flame retardant polyurethane sponge/MTMS aerogel composites with improved mechanical properties under ambient pressure drying. J Nanopart Res 22:221. https://doi.org/10.1007/s11051-020-04958-9

Zhang Y, Wu L, Deng X, Deng Y, Wu X, Shi L, Li M, Liu Q, Cheng X, Li Z (2021) Improving the flame retardance of hydrophobic silica aerogels through a facile post-doping of magnesium hydroxide, Advanced Powder Technology. S0921883121001746. https://doi.org/10.1016/j.apt.2021.03.041

Zhao S, Siqueira G, Drdova S, Norris D, Ubert C, Bonnin A, Galmarini S, Ganobjak M, Pan Z, Brunner S, Nystroem G, Wang J, Koebel MM, Malfait WJ (2020) Additive manufacturing of silica aerogels. Nature 584:387. https://doi.org/10.1038/s41586-020-2594-0